

See discussions, stats, and author profiles for this publication at: <https://www.researchgate.net/publication/229026743>

# Effect of Membrane Surface Roughness on Colloid–Membrane DLVO Interactions

ARTICLE *in* LANGMUIR · MAY 2003

Impact Factor: 4.46 · DOI: 10.1021/la027083c

---

CITATIONS

178

---

READS

167

## 3 AUTHORS:



**Eric MV Hoek**

University of California, Los Angeles

**127** PUBLICATIONS **7,255** CITATIONS

SEE PROFILE



**Subir Bhattacharjee**

Water Planet Engineering

**138** PUBLICATIONS **2,697** CITATIONS

SEE PROFILE



**Menachem Elimelech**

Yale University

**394** PUBLICATIONS **32,554** CITATIONS

SEE PROFILE

# Effect of Membrane Surface Roughness on Colloid–Membrane DLVO Interactions

Eric M. V. Hoek,<sup>\*,†</sup> Subir Bhattacharjee,<sup>‡</sup> and Menachem Elimelech<sup>§</sup>

Department of Chemical and Environmental Engineering, University of California, Riverside, California 92521, Department of Mechanical Engineering, University of Alberta, Edmonton, AB, T6G 2G8, Canada, and Department of Chemical Engineering, Environmental Engineering Program, Yale University, New Haven, Connecticut 06520-8286

Received December 31, 2002. In Final Form: February 26, 2003

Recent experimental investigations suggest that interaction of colloidal particles with polymeric membrane surfaces is influenced by membrane surface morphology (roughness). To better understand the consequences of surface roughness on colloid deposition and fouling, it is imperative that models for predicting the Derjaguin–Landau–Verwey–Overbeek (DLVO) interaction energy between colloidal particles and rough membrane surfaces be developed. We present a technique of reconstructing the mathematical topology of polymeric membrane surfaces using statistical parameters derived from atomic force microscopy roughness analyses. The surface element integration technique is used to calculate the DLVO interactions between spherical colloidal particles and the simulated (reconstructed) membrane surfaces. Predictions show that the repulsive interaction energy barrier between a colloidal particle and a rough membrane is lower than the corresponding barrier for a smooth membrane. The reduction in the energy barrier is strongly correlated with the magnitude of surface roughness. It is further suggested that the valleys created by the membrane surface roughness produce wells of low interaction energy in which colloidal particles may preferentially deposit.

## 1. Introduction

Processes involving interaction of colloidal particles with membrane surfaces have been studied quite avidly over the past decade, leading to considerable insight regarding the dominant particle transport and deposition mechanisms.<sup>1–4</sup> Most of these studies highlight the paramount importance of colloidal interactions, typically represented in terms of the Derjaguin–Landau–Verwey–Overbeek (DLVO) theory, on particle deposition and fouling phenomena. Despite considerable theoretical progress, there appears to be a sizable discrepancy between predictions based on DLVO theory and particle–membrane interaction force measurements,<sup>5</sup> as well as observations pertaining to colloid deposition and fouling.<sup>6–8</sup>

Such departure between theory and experiments has been predominantly ascribed to the presence of other short-range non-DLVO interactions<sup>9,10</sup> and membrane surface roughness.<sup>7,11–13</sup> While non-DLVO interactions are likely to be present in many aquatic systems,<sup>9,10</sup> surface rough-

ness might have an equivalent short-range effect on colloidal interactions.<sup>12</sup> Most previous calculations of particle–membrane DLVO interactions were performed assuming perfectly smooth surfaces of the particles and the membranes.<sup>1,3,4,9</sup> In reality, these entities, particularly the membrane surfaces, cannot be considered as perfectly smooth. Instead, most commercial membrane surfaces are “rough”, displaying significant variability in surface morphology.<sup>14–16</sup>

Experimental investigations suggest that colloid deposition can be enhanced on rough reverse osmosis (RO) and nanofiltration (NF) membrane surfaces.<sup>16,17</sup> For example, atomic force microscopy (AFM) images of fouled membranes show that the initial colloid deposition rate is higher and deposited particles were not evenly distributed on a rough nanofiltration membrane compared to a smooth membrane.<sup>17</sup> Furthermore, recent experimental work using the AFM colloid-probe technique indicates that DLVO interactions between silica particles and rough polymeric membrane surfaces can be strongly influenced by membrane surface roughness.<sup>5,15</sup> In light of these observations, it seems pertinent to quantitatively explore the influence of membrane surface roughness on colloid–membrane interactions through experiments and simulations prior to, or at least concurrently with, postulation of other types of short-range non-DLVO interactions.

Simultaneous measurement of particle–membrane interaction force along with the surface morphology of a

\* Corresponding author. Tel: (909) 787-7345. Fax: (909) 787-5696. E-mail: hoek@engr.ucr.edu.

† University of California.

‡ University of Alberta.

§ Yale University.

(1) Song, L. F.; Elimelech, M. *J. Colloid Interface Sci.* **1995**, *173*, 165–180.

(2) Faibish, R. S.; Elimelech, M.; Cohen, Y. *J. Colloid Interface Sci.* **1998**, *204*, 77–86.

(3) Bacchin, P.; Aimar, P.; Sanchez, V. *AIChE J.* **1995**, *41*, 368–376.

(4) Zydney, A. L.; Pujar, N. S. *Colloids Surf., A* **1998**, *138*, 133–143.

(5) Bowen, W. R.; Doneva, T. A. *J. Colloid Interface Sci.* **2000**, *229*, 544–549.

(6) Elimelech, M.; Gregory, J.; Jia, X.; Williams, R. A. *Particle Deposition & Aggregation: Measurement, Modeling and Simulation*; Butterworth-Heinemann: Woburn, MA, 1995.

(7) Elimelech, M.; O'Melia, C. R. *Langmuir* **1990**, *6*, 1153–1163.

(8) Elimelech, M.; Zhu, X.; Childress, A. E.; Hong, S. *J. Membr. Sci.* **1997**, *127*, 101–109.

(9) Brant, J. A.; Childress, A. E. *J. Membr. Sci.* **2002**, *203*, 257–273.

(10) van Oss, C. J. *Colloids Surf., A* **1993**, *78*, 1–49.

(11) Hirose, M.; Ito, H.; Kamiyama, Y. *J. Membr. Sci.* **1996**, *121*, 209–215.

(12) Bhattacharjee, S.; Ko, C.-H.; Elimelech, M. *Langmuir* **1998**, *14*, 3365–3375.

(13) Walz, J. *Adv. Colloid Interface Sci.* **1998**, *74*, 119.

(14) Kim, J. Y.; Lee, H. K.; Kim, S. C. *J. Membr. Sci.* **1999**, *163*, 159–166.

(15) Bowen, W. R.; Doneva, T. A.; Stoton, A. G. *Colloids Surf., A* **2002**, *201*, 73–83.

(16) Zhu, X.; Elimelech, M. *Environ. Sci. Technol.* **1997**, *31*, 3654–3662.

(17) Vrijenhoek, E. M.; Elimelech, M.; Hong, S. *J. Membr. Sci.* **2001**, *188*, 115–128.

membrane using atomic force microscopy has provided considerable experimental insight into how the interaction forces are modified by surface roughness. In particular, the colloid-probe technique has become popular in recent years for characterization of the colloid–membrane interaction force. While the colloid-probe technique presents a powerful experimental method for characterizing particle–membrane surface interactions, the resolution of this technique is limited by the rather large size of the colloidal probes, which may be several orders of magnitude larger than membrane surface roughness features. On the basis of presently available techniques, only particles larger than about 1  $\mu\text{m}$  can be attached to an AFM cantilever. The radius of curvature of such a large probe fails to provide adequate resolution of the nanoscale topological features engendered by roughness. An alternative to the colloid-probe technique is to perform a scan of the membrane using a regular AFM probe with very small tip radius to assess the “exact” topology of its surface. Following this, the interaction energy between a spherical particle of any size and the rough membrane surface can be calculated in the framework of the DLVO theory by taking into consideration the AFM-imaged topology of the membrane. Such an approach will provide a more realistic mapping of the interaction energies and forces at different locations of the membrane surface. Although such an approach underlies the so-called force–volume technique using a colloidal probe, the methodology delineated above obviates the attachment of a large colloidal probe to the AFM cantilever and conceptually allows determination of interaction forces on colloidal particles that are smaller than the membrane roughness features.

This paper presents a technique of reconstructing a mathematical topology of membrane surfaces using information from AFM scans of polymeric (nanofiltration and reverse osmosis) membranes and evaluating the DLVO interaction energy between a colloidal particle and the reconstructed rough membrane. The surface element integration (SEI) technique<sup>18</sup> is used to calculate the DLVO interaction energy between colloids and the reconstructed rough membrane surfaces. The interaction energy profiles for the rough membranes are compared with the corresponding estimates for perfectly planar membrane surfaces to assess the influence of roughness on the DLVO interaction energy. Interaction energy calculations at various horizontal and vertical locations above the rough surfaces are obtained to map the interaction energy over a small slice of the membrane in a manner analogous to a “force–volume” data set acquired using AFM.<sup>19</sup> These interaction energy maps are used to highlight the significance of membrane surface roughness on dictating the deposition behavior of approaching colloidal particles.

## 2. Mathematical Modeling

The primary goal of the present study is to obtain a quantitative understanding of the effect of membrane surface roughness on colloid–membrane DLVO interactions. These calculations may then shed some light on the role of membrane surface morphology on particle deposition. However, before embarking on any mathematical modeling, it should be noted that the geometric complexity of rough surfaces precludes a *rigorous* computation of the interaction energy between such a surface and a particle. The primary problem stems from the randomness of surface roughness, which is difficult to represent consis-

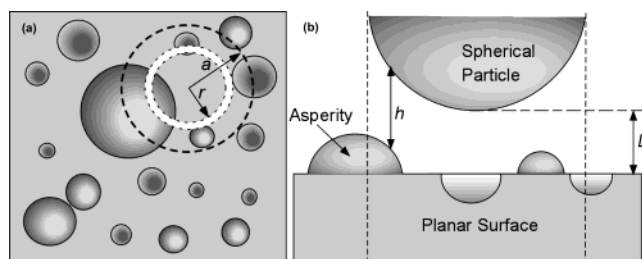


**Figure 1.** Illustration of (a) the radial surface area mapping technique and (b) the surface-to-surface separation distance used in SEI calculations. In (a), the dashed circle outlines the “shadow” of the traveling sphere on the mean-plane, and its radius is given as  $a$ . In (b), the separation distance from the leading edge of the sphere to the mean-plane is labeled  $D$ , while the local separation distance is labeled  $h$ .

tently using any mathematical model. This problem might be circumvented to some extent by basing any mathematical approach for evaluation of the interaction energy on a hypothetical surface topology that represents some pertinent statistical properties of the rough surface. The second problem stems from the fact that rough surfaces preclude using any form of symmetry while evaluating the interaction energy. For instance, employing Hamaker’s approach to determine the van der Waals interaction between two macrobodies of arbitrary shapes requires evaluation of six nested integrals. Similarly, rigorous evaluation of the electrostatic double-layer interaction between two particles of arbitrary geometry requires numerical solution of the Poisson–Boltzmann (PB) equation, with the nonuniform surfaces approximated through some spatial discretization procedure (typically finite difference or finite element meshes). With a wide variation of roughness feature (asperity) size, the resulting spatial discretization must be adaptive, so that all the features of the rough surface are captured in the solution of the PB equation. Such a computation is numerically cumbersome and would require substantial computation time. These numerical limitations may be avoided, albeit at the expense of some accuracy, by using the SEI technique.

**2.1. Surface Element Integration.** The SEI technique considers the total interaction energy between two bodies by integrating the interaction energy per unit area between two infinite planar surfaces over the actual surfaces.<sup>18</sup> The integration procedure, which is similar in principle to Derjaguin’s approximation (DA),<sup>20,21</sup> is applied to the exact geometry of the interacting surfaces. The basic governing equation of SEI applicable to the scenario of a spherical particle interacting with a rough planar surface is

$$U(D) = \int \int_{\text{particle}} E(h) \, dA \quad (1)$$

Here  $U$  is the interaction energy between the particle and the rough surface,  $D$  is the distance of closest approach between the sphere and the mean-plane of the rough surface,  $E$  is the interaction energy per unit area between two infinite planar surfaces separated by a distance  $h$ , and  $dA$  is a projected differential surface area of the particle.<sup>22</sup>

To provide a facile description of the mathematical formulation, we base the following discussion on a model of the rough surface comprising hemispherical asperities as shown in Figure 1. In this figure, we depict a model

(18) Bhattacharjee, S.; Elimelech, M. *J. Colloid Interface Sci.* **1997**, *193*, 273–285.

(19) Rotsch, C.; Radmacher, M. *Langmuir* **1997**, *11*, 2825–2832.

(20) Derjaguin, B. V. *Kolloid-Z.* **1934**, *69*, 155–164.

(21) White, L. R. *J. Colloid Interface Sci.* **1983**, *95*, 286–288.

(22) Bhattacharjee, S.; Elimelech, M.; Borkovec, M. *Croat. Chem. Acta* **1998**, *71*, 883–903.

rough surface containing a distribution of hemispherical protrusions and depressions of different radii (Figure 1a) interacting with a smooth spherical particle of radius  $a$  located at a vertical distance  $D$  from the mean-plane of the rough surface (Figure 1b). We note that  $D$  represents the distance of closest approach between the sphere surface and the mean-plane of the rough surface. The analysis presented here employs a cylindrical coordinate system, with the origin located at the center of the spherical particle. In this coordinate frame, the expression for the interaction energy becomes

$$U(D) = \int_0^{2\pi} \int_0^a E(h) r dr d\theta \quad (2)$$

where  $h$  is the vertical distance between a circular arc (differential surface area  $r dr d\theta$ ) of the particle surface and the point on the rough surface directly below it. The evaluation of the surface integral, eq 2, requires representation of the distance  $h$  as a function of  $r$  and  $\theta$ . The distance  $h(r, \theta)$  will depend on the distribution of the asperity centers relative to the center of the traveling sphere. The surface integral in eq 2 is evaluated over the area directly under the traveling sphere. Hence, only the regions of the asperities that overlap with the projected area of the traveling sphere (i.e., within the dashed circle in Figure 1a) are considered in the energy computation.

A suitable expression for the interaction energy per unit area between two infinite flat plates (separated by a distance  $h$ ) is required to obtain the interaction energy between the traveling sphere and the rough surface. In this study, we use the DLVO interaction energy per unit area between two infinite planar surfaces obtained by adding the Hamaker expression for the van der Waals interaction and the constant potential electrostatic double-layer interaction energy expression.<sup>22,23</sup> The total DLVO interaction energy per unit area between differential elements of the surfaces is thus given by

$$E_{\text{DLVO}}(h) = E_{\text{VDW}}(h) + E_{\text{EDL}}(h) = -\frac{A_H}{12\pi h^2} + \frac{\epsilon\epsilon_0\kappa}{2} \left[ (\psi_s^2 + \psi_m^2)(1 - \coth \kappa h) + \frac{2\psi_s\psi_m}{\sinh \kappa h} \right] \quad (3)$$

Here  $A_H$  is the Hamaker constant of the interacting media,  $\epsilon_0$  is the dielectric permittivity of vacuum,  $\epsilon$  is the dielectric constant of the solvent,  $\kappa$  is the inverse Debye screening length, and  $\psi_s$  and  $\psi_m$  are the surface potentials of the sphere and the membrane, respectively. Substituting this expression into eq 2 yields the interaction energy between the spherical particle and the membrane surface.

The surface element integration provides the interaction energy between the spherical particle and the rough surface for each location of the sphere center. Shifting the horizontal location of the sphere center with respect to the rough membrane surface yields a map of the interaction energy experienced by this particle as it samples the terrain of the rough membrane. In the following subsection, the technique of obtaining such a detailed map of the interaction energy as the spherical particle travels over the entire expanse of the rough membrane surface is described.

**2.2. Calculation of the Sphere–Rough Surface Interaction Energy.** The center of the traveling sphere is fixed relative to the membrane surface and assigned location coordinates  $(x_c, y_c)$ . For each location of the particle

center, the numbers of asperities and the regions of each asperity on the membrane that intersect with the projected area of the sphere are determined, employing the following inequality:

$$(x_i - x_c)^2 + (y_i - y_c)^2 < (a + a_i)^2 \quad (4)$$

where  $(x_i, y_i)$  and  $a_i$  represent the coordinates of the center and the radius of the  $i$ th asperity, respectively (Figure 1). While the cylindrical polar coordinate system is employed to evaluate the surface integral, eq 2, the distance  $h$  is determined using a global Cartesian coordinate system. The calculation of the interaction energy is confined only to the segments of the asperities that satisfy eq 4.

Considering the center of the traveling sphere as the origin, the vertical distance between a surface element on the particle and the region of the membrane surface directly below it is

$$h = D + a - \sqrt{a^2 - r^2} - \sqrt{a_i^2 - r_i^2} \quad \text{for a protrusion} \quad (5)$$

$$h = D + a - \sqrt{a^2 - r^2} + \sqrt{a_i^2 - r_i^2} \quad \text{for a depression}$$

where  $r_i$  is the radial distance of the asperity surface from the center of the asperity. Equation 5 should be applied when the particle surface does not overlap with the space occupied by a protruding asperity. This condition can be stated as

$$(x - x_i)^2 + (y - y_i)^2 > a_i^2 \quad (6)$$

where  $(x, y)$  are the coordinates of the spherical surface under consideration, and  $(x_i, y_i)$  are the coordinates of the asperity center. Equation 6 simply states that the distance between the spherical surface and the center of a protruding hemispherical asperity must be greater than the asperity radius to ensure that there is no physical overlap. Equation 5 can be represented as

$$h = D + a - \sqrt{a^2 - r^2} \quad (7)$$

when there is no asperity directly below a surface element of the traveling sphere.

The interaction energy per unit area corresponding to  $h$  for each  $(r, \theta)$  is then evaluated for the specified functional dependence of  $E$  on  $h$  (eq 3). Integrating this interaction energy over the surface of the sphere facing the rough plane yields the total interaction energy between the traveling sphere and the rough surface.

Since the separation distance ( $D$ ) is defined from the mean-plane, there may be instances where portions of the particle will overlap with a volume of space occupied by a protruding (positive) asperity. Mathematically, this presents a problem because at some points along the surface of the particle the local separation distance ( $h$ ) can assume a value of zero or even negative values. Such an unphysical situation will render the local van der Waals attraction infinite (see eq 3). Since it is physically impossible for a particle to occupy a position where it overlaps with an asperity, the unrealistic interaction energies are simply omitted from the present calculations. This point will be further clarified in section 4.

The raster scan of a rough surface by a colloidal probe can now be simulated by assigning different horizontal locations of the sphere center  $(x_c, y_c)$  along a predefined grid and repeating the energy calculations for each of these locations. An alternative set of calculations can be

(23) Hogg, R. I.; Healy, T. W.; Fuerstenau, D. W. *Trans. Faraday Soc.* **1966**, *62*, 1638–1651.



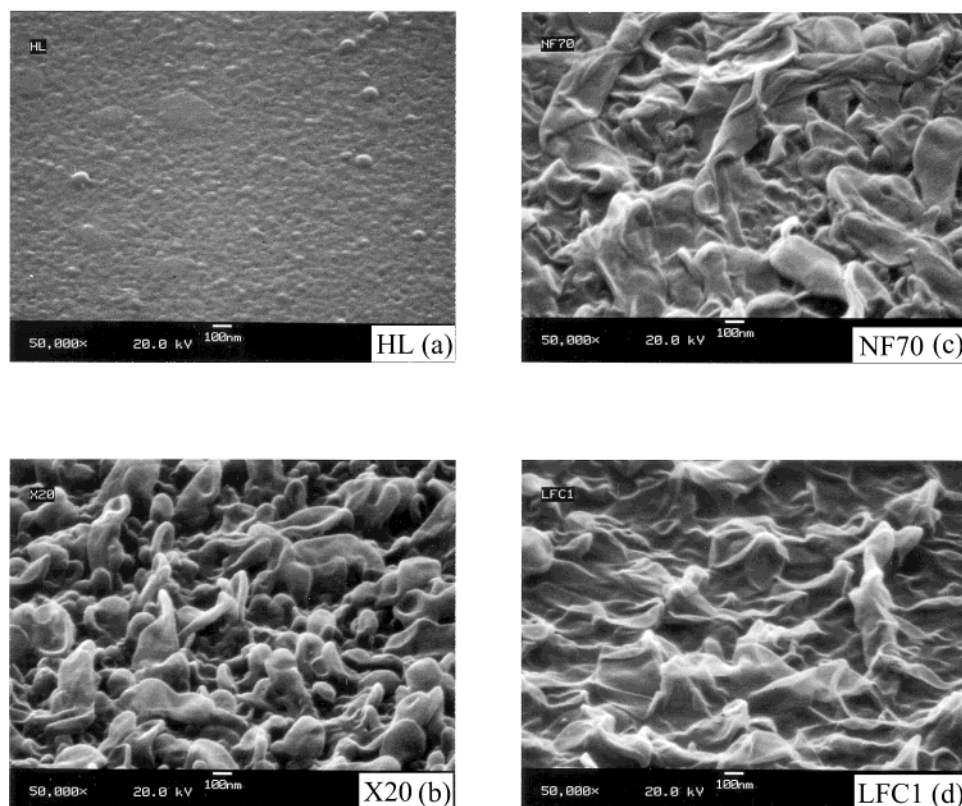


**Figure 2.** FESEM images of real polymeric thin-film composite membranes (a) HL, (b) X20, (c) NF70, and (d) LFC1 used as the basis for modeling particle–membrane interactions. The magnification is 50 000 $\times$ , the accelerating voltage is 20 kV, the photo angle is 45° from normal, and the scale bar is 100 nm in length. Note the different surface morphologies: (a) small, closely spaced hemispherical asperities, but relatively smooth; (b) large, closely spaced, lobelike asperities; (c) large, widely spaced folded-lobe asperities; and (d) large, widely spaced, ridge-and-valley type asperities.

performed, where the particle is assigned a single  $(x_c, y_c)$  location and the separation distance ( $D$ ) is varied from near contact to a distance where  $E(h)$  shows little or no change with increasing separation.

### 3. Characterization of Membrane Surface Roughness

#### 3.1. Membrane and Colloid Surface Properties.

The membrane properties used to generate simulated membrane surfaces were taken from four commercial RO/NF polyamide thin-film composite membranes. The RO membranes were designated by the manufacturer as LFC1 (Hydranautics, Oceanside, CA) and X20 (Trisep, Goleta, CA). The NF membranes were designated as NF70 (Dow-FilmTec, Minneapolis, MN) and HL (Osmonics, Minnetonka, MN). Clean membrane samples were imaged by field emission scanning electron microscopy (FESEM) and surface roughness was determined by AFM. The FESEM sample preparation and imaging were performed following the method described by Kim et al.<sup>24</sup> The FESEM images were acquired at an accelerating voltage of 20 kV and 500–100 000 times magnification. Imaging and roughness analysis via AFM were performed for dry membranes in air using “tapping mode” as described elsewhere.<sup>17</sup> The surface (zeta) potential of the membranes was determined at a solution ionic strength of 10 mM (NaCl) and a pH value of 7 using streaming potential measurements. Details of these measurements were reported elsewhere.<sup>17</sup> The measured membrane zeta potentials were  $-13$  mV for LFC1,  $-18$  mV for HL,  $-20$  mV for X20, and  $-25$  mV for NF70. A surface potential of  $-25$  mV was assigned to

the model colloids in our simulations based on the zeta potential for silica colloids at 10 mM ionic strength and pH 7 determined experimentally elsewhere.<sup>17</sup>

**3.2. FESEM and AFM Membrane Surface Analyses.** Figure 2 shows FESEM images of the four RO/NF membranes taken at a 45° angle. The HL surface is relatively smooth, compared to the other three membranes. It is clear from these images that the four membranes exhibit a range of surface morphologies. In particular, the size and shape of roughness features (asperities) are very different: HL has many small asperities that may be best described as half oblate-spheroids, X20 has a large number of lobelike structures over a range of sizes, and NF70 and LFC1 exhibit relatively fewer (in number) but larger foldlike protuberances. Also, the roughness features on LFC1 and NF70 are spaced apart as much as 1  $\mu\text{m}$  between major peaks, whereas X20 has a much smaller peak-to-peak separation distance ( $<100$  nm from visual inspection of several FESEM images).

Representative orthographic plots of tapping mode AFM images for the four RO/NF membranes are presented in Figure 3. Some details regarding the shape of individual asperities are lost in the AFM images, but the general morphological trend is preserved. HL appears smooth, X20 has moderately sized and closely spaced roughness features, and LFC1 and NF70 have large, widely spaced features. In the AFM images, the roughness features appear exaggerated due to the aspect ratio of the figure (the vertical scale is only 500 nm per division, while the  $x$  and  $y$  scales are 2  $\mu\text{m}$  per division).

**3.3. AFM-Based Statistics of Surface Roughness.** FESEM images provide fine resolution of individual asperities, but inspection of surfaces by AFM provides a

(24) Kim, K. J.; Dickson, M. R.; Chen, V.; Fane, A. G. *Micron Microsc. Acta* **1992**, *23*, 259–271.

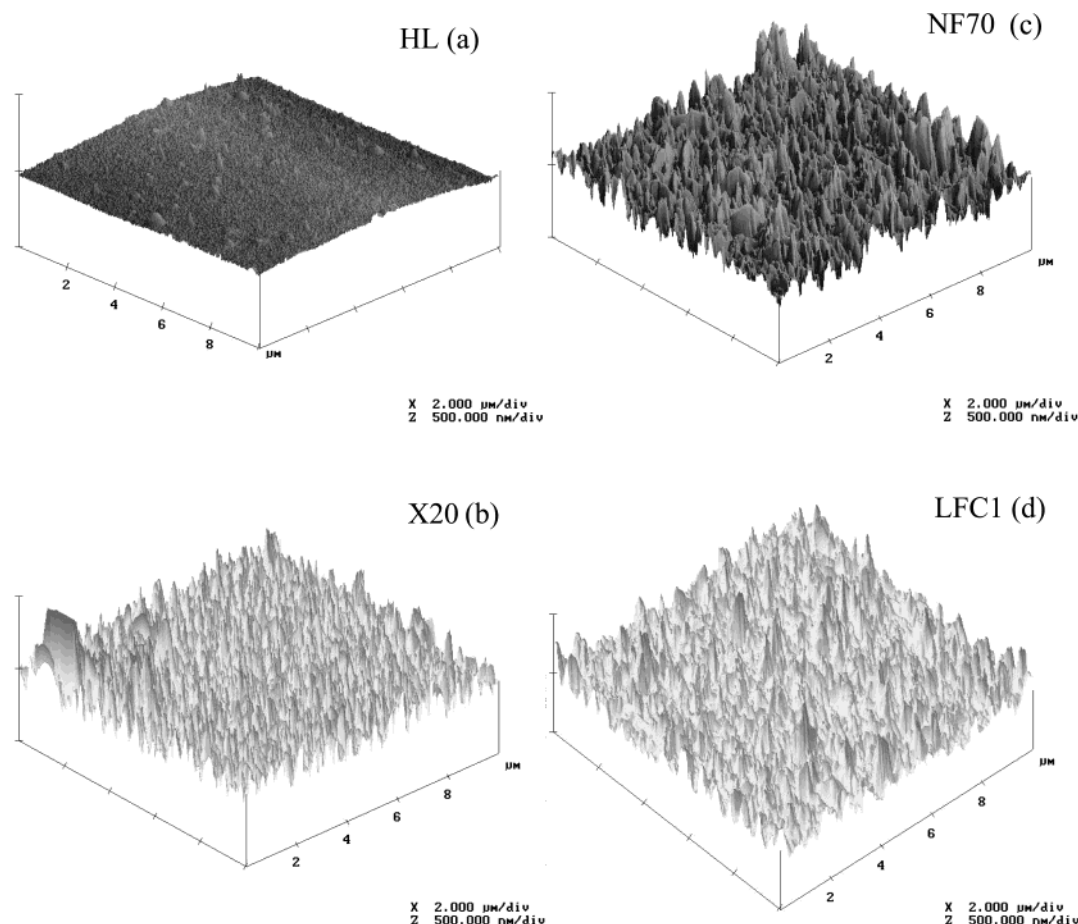


**Figure 3.** AFM images showing the surfaces of (a) HL, (b) X20, (c) NF70, and (d) LFC1 membranes. The AFM images lack the resolution of the SEM images of Figure 2 and cannot capture the exact shape of surface roughness features, but the magnitude and periodicity of roughness features are retained: (a) small, closely spaced asperities, but relatively smooth; (b) large, closely spaced asperities; and (c,d) large, widely spaced asperities. The vertical scale is enhanced to amplify the surface morphology of the membranes (500 nm/division for  $Z$ -scale compared to 2  $\mu\text{m}$  per division for  $X$  and  $Y$ ), and the scan area is 10  $\mu\text{m} \times 10 \mu\text{m}$ .

**Table 1. Average Measured Membrane Surface Properties via AFM and EKA**

| morphological parameter           | units | HL    | X20   | NF70  | LFC1  |
|-----------------------------------|-------|-------|-------|-------|-------|
| mean, $m$                         | nm    | 0.065 | 0.049 | 0.147 | 0.121 |
| average roughness, $R_a$          | nm    | 10.1  | 33.4  | 43.3  | 52.0  |
| rms roughness, $R_q$              | nm    | 12.8  | 41.6  | 56.5  | 67.4  |
| maximum roughness, $R_m$          | nm    | 129   | 373   | 577   | 574   |
| peak count, PC                    |       | 545   | 859   | 210   | 146   |
| surface area difference, SAD      | %     | 1.70  | 33.0  | 20.7  | 16.9  |
| surface (zeta) potential, $\zeta$ | mV    | -18   | -20   | -25   | -13   |

statistical analysis of surface roughness features. In the AFM roughness analysis, a mean-plane of length  $X$  and width  $Y$  defines the surface. Morphological features are defined by  $x$ ,  $y$ , and  $z$  coordinates, which indicate the relative height ( $z$ ) of the cantilever tip at each  $x$  and  $y$  planar location. The following AFM "roughness analysis" parameters were chosen as key descriptors of membrane surface morphology: mean ( $m$ ), average roughness ( $R_a$ ), root-mean-square (rms) roughness ( $R_q$ ), surface area difference (SAD), and peak count (PC). The key membrane surface roughness statistics for the four RO/NF membranes considered in this study are listed in Table 1.

The mean value is defined as the arithmetic mean of all height data obtained from an AFM surface scan. The mean value ( $m$ ) represents the absolute  $z$ -value of the mean-plane that is drawn through the cross section of peaks and valleys for a rough surface. The calculated  $m$  is typically nonzero because all data points are measured with respect to the starting elevation of the AFM probe tip, which is arbitrary. However, for the large surface areas

analyzed in this study the mean value was quite small (ca. 0.1 nm).

Average roughness ( $R_a$ ) measured by AFM is the average deviation of the measured  $z$ -values from the mean-plane. For the membrane surfaces,  $R_a$  may be thought of as half the average peak-to-valley depth. The data in Table 1 are listed in order of increasing average roughness: HL (10 nm), X20 (33 nm), NF70 (43 nm), and LFC1 (52 nm).

Root-mean-square roughness ( $R_q$ ) effectively describes the standard deviation of an entire distribution of  $z$ -values for a large sample size. For the membranes tested, the  $R_q$  values increase in the same order as average roughness and are larger in magnitude than the average roughness value.

Maximum roughness ( $R_m$ ) indicates the difference between the largest positive and negative  $z$ -values. This does not indicate that any peak-to-valley depth of this magnitude exists, but more accurately provides quantification of the spread of the distribution of measured asperity heights. The same is true of the  $R_m$  values calculated for the simulated surfaces. Interestingly, the maximum roughness for the NF70 surfaces was the largest, whereas LFC1 appears to be the roughest on average.

The surface area difference (SAD) is the increase in surface area, due to roughness, over a flat plane with the same  $X$  and  $Y$  dimensions. The SAD is a critical parameter that describes the accumulated surface area of all roughness features on a sample. In the simulated surfaces, the surface area of individual asperities is directly calculated

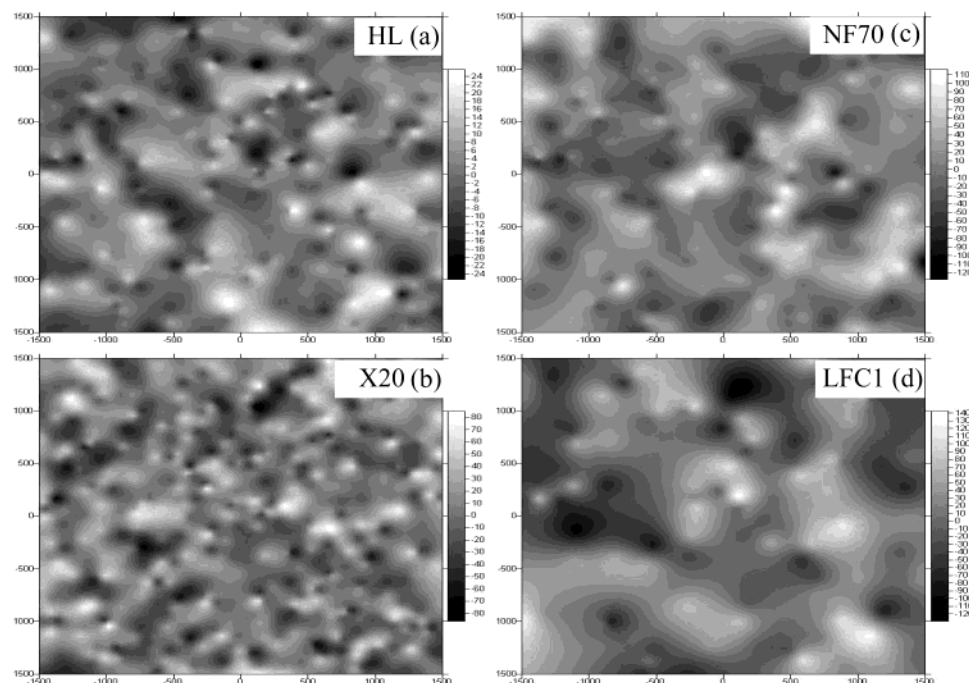


**Figure 4.** Plan view images of  $9\ \mu\text{m}^2$  SIM membrane surfaces reconstructed from AFM roughness statistics listed in Table 1 for (a) HL, (b) X20, (c) NF70, and (d) LFC1. The surface morphologies are reproduced in the SIM surfaces: (a) small, closely spaced asperities; (b) large, closely spaced asperities; and (c,d) large, widely spaced asperities. Note that the vertical scales are enhanced to highlight the location of individual asperities. The  $X$ - and  $Y$ -scales range from  $-1500$  to  $+1500$  nm on all four images, while the  $Z$ -scales are (a)  $\pm 25$  nm, (b)  $\pm 125$  nm, (c)  $\pm 85$  nm, and (d)  $\pm 140$  nm.

and the sum over all asperities divided by the equivalent flat plate surface area provides the SAD value. The SAD of a sample surface encompasses the size and number of asperities per unit area, which determines the periodicity (or spacing) of asperities. The peak-to-peak separation may strongly influence the nature of colloid–membrane interactions, especially when the particle size is larger than the average peak-to-peak separation, which is the case for X20 in particular. Thus, although LFC1 and NF70 are on average significantly “rougher”, the X20 surface exhibits more than double the SAD.

The peak count (PC) is defined as the number of “peaks” that are larger in absolute value than one standard deviation from the mean, or the magnitude of  $R_q$ . A peak is defined by AFM as being the highest  $z$ -value among a defined number of surrounding  $z$ -values. This definition is necessary because on the real surfaces a large peak may have smaller peaks along its sides. However, peaks and valleys with well-defined shape are used on simulated surfaces, so the height and surface area can easily be computed. The peak count gives an estimate of the shape of the overall distribution of  $z$ -values (short and wide, tall and narrow).

#### 4. DLVO Interaction between a Colloidal Particle and a Model Rough Surface

**4.1. A Simple Roughness Model for Calculation of DLVO Interaction.** The statistical parameters from the AFM roughness analyses of the four membranes were used as inputs to simulate model rough surfaces. For simplicity, and in conformity with the interaction energy model discussed in the theoretical section, the simulated surfaces were composed of a perfectly flat plane, interrupted by positive and negative hemispheres, which formed the peaks and valleys.

The creation of the simulated rough surfaces began with the use of the AFM-measured  $R_a$  value as the average height (or radius) of a hemispherical asperity. The surface

area of the resulting hemisphere determined the average asperity surface area. The AFM-measured SAD value (expressed as a percent) was multiplied by the simulated flat surface area ( $X \times Y$ ) and divided by the average asperity surface area to provide an initial guess for the number of asperities ( $n$ ). A normal distribution of  $n$  values was generated with a mean equal to zero and unit standard deviation. Each value in the  $n$ -sized sample was then multiplied by the AFM-measured  $R_q$  value to obtain the distribution of the radii of the hemispherical asperities. The surface area of each asperity of the distribution was calculated, and the sum was compared to the AFM-measured SAD values. The number of asperities was adjusted and the previous steps were repeated, until the difference between simulated (SIM) and measured (AFM) SAD values was minimized. The asperities were then randomly placed on the flat plate such that no asperity overlapped with another. For large samples ( $n \rightarrow \infty$ ), the resulting distribution had (by design) a mean of zero and standard deviation  $R_q$ . However, the number of asperities was limited by fitting to the AFM-measured roughness parameters. The finite sample size resulted in minor deviations from the AFM-measured  $R_a$  and  $R_q$  values but significant deviation from measured PC and  $R_m$  values. This is the primary source of error in recreating the roughness statistics of measured (AFM) parameters using asperities of well-defined geometric shapes (hemispheres in this case).

Figure 4 depicts the reconstructed topologies of the four types of membranes obtained from their respective AFM statistics. These simulated surfaces were generated for a  $3\ \mu\text{m} \times 3\ \mu\text{m}$  projected surface area. The lighter regions represent the peaks, while the darker regions represent the valleys or depressions on the surface. These simulated surfaces do not resemble the actual topology of the membranes. Only the statistical roughness parameters obtained from the AFM scans of the real membranes are matched in these reconstructed surfaces. The subsequent



**Table 2. Measured and Simulated Membrane Statistical Roughness Parameters (Hemispheres)**

| morphological parameter           | units           | HL               |                  | X20              |                  | NF70             |                  | LFC1             |                  |
|-----------------------------------|-----------------|------------------|------------------|------------------|------------------|------------------|------------------|------------------|------------------|
|                                   |                 | AFM <sup>a</sup> | SIM <sup>b</sup> | AFM <sup>a</sup> | SIM <sup>b</sup> | AFM <sup>a</sup> | SIM <sup>b</sup> | AFM <sup>a</sup> | SIM <sup>b</sup> |
| membrane area                     | $\mu\text{m}^2$ | 100              | 9                | 100              | 9                | 100              | 9                | 100              | 9                |
| number of asperities ( <i>n</i> ) | no.             | N/A <sup>c</sup> | 417              | N/A <sup>c</sup> | 748              | N/A <sup>c</sup> | 277              | N/A <sup>c</sup> | 157              |
| average roughness, Ra             | nm              | 10.1             | 8.7              | 33.4             | 28.4             | 43.3             | 37.0             | 52.0             | 44.7             |
| rms roughness, Rq                 | nm              | 12.8             | 10.8             | 41.6             | 35.0             | 56.5             | 45.7             | 67.4             | 55.1             |
| maximum roughness, Rm             | nm              | 129              | 61               | 373              | 201              | 577              | 259              | 574              | 301              |
| peak count, PC                    | no.             | 545              | 136              | 859              | 251              | 210              | 93               | 146              | 57               |
| surface area difference, SAD      | %               | 1.70             | 1.71             | 32.7             | 32.8             | 20.7             | 20.5             | 16.9             | 16.9             |

<sup>a</sup> Surface area scanned and analyzed by AFM. <sup>b</sup> Surface area reconstructed using hemispherical asperities. <sup>c</sup> The number of asperities in AFM surface scans was not determined.

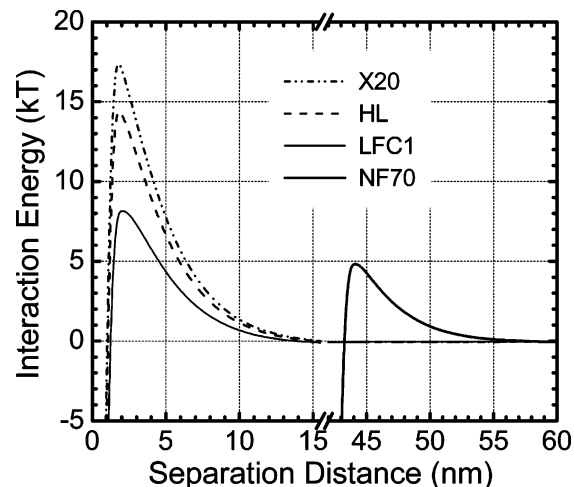
calculations of the DLVO interaction energies between a spherical particle and the four types of rough membranes will be performed on the basis of these simulated topologies.

Table 2 lists the statistical roughness parameters obtained from the AFM roughness analysis (AFM) and the model rough surface with hemispherical asperities (SIM). Comparison between the statistics for the AFM measurements and the simulated rough surfaces indicates that the SAD values for both the AFM and SIM surfaces are in good agreement, while the Ra and Rq values for the simulated surfaces were somewhat smaller than those of the actual membranes.

**4.2. Interaction between a Colloidal Particle and a Model Rough Surface.** The following discussion presents two approaches for comparing the influence of surface roughness on colloid–membrane DLVO interactions. First, the interaction energy versus distance profile was determined at several *x,y* locations on each simulated rough surface. The average values for each membrane were compared to each other and to values for equivalently charged smooth surfaces. Second, the interaction energy was computed at several separation distances spanning the entire surface. Interaction energy maps were then plotted for several different separation distances between the probe particle and the mean-plane of the rough surface to reveal the potential influence of membrane surface roughness on the deposition behavior of a particle approaching the surface. In all these simulations, the probe particle was assigned a radius of 50 nm.

**4.2.1. Influence of Surface Roughness on the DLVO Interaction Energy Barrier.** Comparing the interaction energy versus distance profile at a single (*x,y*) location was particularly challenging because roughness features were close in size to the particle radius. The DLVO interaction energy barrier at an arbitrary (*x,y*) location was computed by moving the particle from the mean-plane to a large separation distance ( $> 100$  nm) in 0.25 nm increments. Figure 5 presents interaction energy versus separation profiles for the four membranes. All simulations pertain to an ionic strength of 0.01 M (1:1 electrolyte), the Hamaker constant  $4.1 \times 10^{-21}$  J, and a particle surface potential of  $-25$  mV.

Direct comparison of interaction energy profiles in Figure 5 reveals little about the sole influence of surface roughness because each of these profiles resulted from a different surface morphology and a different surface (zeta) potential. However, it is particularly interesting that the membrane (NF70) with the most negative zeta potential produces the smallest primary energy barrier. This occurred because there was a large positive asperity at that (*x<sub>c</sub>, y<sub>c</sub>*) location which physically prevented the particle from attaining a separation distance of less than 43 nm from the mean-plane. This specifically illustrates the limitation of comparing interactions between a particle and rough surface at a single location. In general, the



**Figure 5.** SEI model predictions of interaction energy profiles for a 50 nm (radius) sphere and the simulated membrane surfaces of Figure 4. The simulation ionic strength was  $10^{-2}$  M (1:1 electrolyte) at neutral pH, and the membrane surface (zeta) potentials were  $-13$  mV (LFC1),  $-18$  mV (HL),  $-20$  mV (X20), and  $-25$  mV (NF70). The simulated colloid surface potential was  $-25$  mV. A large asperity on the NF70 surface prevented the particle from approaching closer than  $\sim 43$  nm away from the mean-plane.

interaction energy decays from a maximum (the primary energy barrier) to zero over a distance of about 12 nm for all surfaces. This is true even if an interfering asperity prevents the particle from reaching the mean-plane of the membrane surface as occurred for NF70.

The simulations described above were then repeated for 10 additional randomly selected (*x,y*) locations. The interaction energy barrier heights from all these calculations for a given membrane were averaged, and a summary of these results is presented in Table 3. The last three columns of the table provide the average energy barrier,  $U_{\text{avg pk}}$ , the energy barrier for a perfectly flat surface bearing the same surface potential as the membranes considered,  $U_{\text{FP pk}}$ , and the percentage reduction in the barrier height (due to roughness) for each membrane,  $\Delta U_{\text{pk}}$ .

For all the surfaces, the presence of roughness features reduces the interaction energy barrier compared to that of a planar surface. As expected, the average rough surface energy barrier and the flat plate energy barrier heights correlated well with the membrane surface zeta potential ( $\zeta$ ), but the reductions in the average primary energy barrier ( $\Delta U_{\text{pk}}$ ) due to roughness were best correlated with the magnitude of surface roughness features (Ra, Rq, Rm). Interestingly, the periodicity of roughness features, captured by the surface area difference (SAD) value, was not strongly correlated to the reduction in the primary energy barrier. In summary, for rough surfaces, the interaction energy barrier height is primarily determined



**Table 3. Influence of Membrane Surface Properties on the Primary Energy Barrier<sup>a</sup>**

|   | $\zeta$ (mV) | $N$ (no.) | Ra (nm)      | Rq (nm)      | Rm (nm)      | SAD (%) | PC   | $U_{\text{FP pk}}$ (kT) | $U_{\text{avg pk}}$ (kT) | $\Delta U_{\text{pk}}$ |
|---|--------------|-----------|--------------|--------------|--------------|---------|------|-------------------------|--------------------------|------------------------|
| LFC1                                      | −13          | 157       | 45           | 55           | 301          | 16.9    | 57   | 8.7                     | 6.8                      | −21.9%                 |
| HL  | −18          | 417       | 9            | 11           | 61           | 1.71    | 136  | 15.8                    | 14.6                     | −7.8%                  |
| X20                                       | −20          | 748       | 28           | 35           | 201          | 32.8    | 251  | 18.7                    | 14.7                     | −21.0%                 |
| NF70                                      | −25          | 277       | 37           | 46           | 259          | 20.5    | 93   | 25.7                    | 18.2                     | −29.3%                 |
| correlation with $\zeta^b$                | <b>−1.00</b> |           |              |              |              |         |      | <b>−1.00</b>            | <b>−0.95</b>             | 0.43                   |
| correlation with $U_{\text{avg pk}}^c$    | <b>−0.95</b> | 0.41      | −0.40        | −0.40        | −0.36        | 0.11    | 0.39 |                         |                          |                        |
| correlation with $\Delta U_{\text{pk}}^d$ | 0.43         | 0.21      | <b>−0.84</b> | <b>−0.84</b> | <b>−0.87</b> | −0.69   | 0.19 |                         |                          |                        |

<sup>a</sup> Key: the particle  $\zeta$  was −25 mV assuming  $I = 0.01$  M (1:1 electrolyte) at pH = 7; roughness statistics are SIM data from Table 2;  $U_{\text{FP pk}}$  = the colloid–flat plate interaction energy barrier height;  $U_{\text{avg pk}}$  = the average colloid–membrane interaction energy barrier height;  $\Delta U_{\text{pk}}$  = the change in the interaction energy barrier height due to roughness. <sup>b</sup> Correlation coefficient between the zeta potential and the calculated interaction energy barrier. <sup>c</sup> Correlation coefficient between  $U_{\text{avg pk}}$  and columnar data. <sup>d</sup> Correlation coefficient between  $\Delta U_{\text{pk}}$  and columnar data.

by the zeta potentials of the surfaces, but the extent of deviation of the energy barrier height from the corresponding sphere–flat plate energy barrier is controlled by the magnitude of the roughness.

**4.2.2. Influence of Surface Roughness on Local Interaction Energy and Particle Deposition.** Computing particle–membrane interactions at a particular separation distance and over a range of  $x, y$  locations allowed plotting of an interaction energy map over the surface. This was done by varying the horizontal positions ( $x, y$ ) of the probe particle center in a rasterized manner by keeping the vertical distance ( $z$ ) between the particle center and the mean-plane of the membrane fixed. When this was performed over a series of vertical distances, the interaction energy equivalent of an AFM force–volume data set was produced.

A typical problem encountered during these simulations stemmed from the divergence of the van der Waals interaction due to physical overlap between the probe particle and a protruding asperity from the simulated rough surface. This physically untenable situation was handled by simply avoiding any computation of energy for particle center locations that would lead to such physical overlap. Simulation conditions for the interaction energy–volume data sets were identical to those described above.

The interaction energy maps for the four model rough surfaces conforming to the AFM statistics of the RO/NF membranes are shown in Figures 6–9. Each numbered figure pertains to a different simulated membrane surface, while the four maps (parts a–d) in each of the figures correspond to a different fixed colloid probe–mean-plane separation distance ranging from (a) 50 nm down to (d) 5 nm. The gray-scale portions of each map are the underlying membrane surface image of Figure 4, while the superimposed color map shows the interaction energy distribution on the surface. The gray-scale regions also indicate the locations where the interaction energy could not be determined due to physical overlap between the particle and the asperity. It is realistic to ignore the interaction energy in these regions because it is physically impossible for any part of a colloidal particle to occupy a volume of space that is occupied by the membrane surface. Areas mapped in blue indicate negative (attractive) interaction energy, and areas mapped in red indicate positive (repulsive) interaction energy. Neutral or zero interaction energy is depicted in purple. The scale bar to the right of each plot represents the interaction energy in units of  $kT$ .

Figure 6a–d depicts the interaction energy maps for a simulated HL membrane. The simulated HL surface is composed of many small asperities, the radii of which are small with respect to the probe particle radius of 50 nm. As the 50 nm radius particle scans the simulated HL

membrane, it feels weak attractive interaction energy ( $<0.01$   $kT$ ) at a separation of 50 nm (Figure 6a). An interesting point here is that at 50 nm separation, the colloid feels an elevated attraction by several positive asperities. The particle is being “sucked” into the secondary minimum surrounding the peaks. At some vertical distance between 50 and 25 nm from the mean-plane, a particle with enough convective energy pushes through the secondary minimum and begins to experience electrostatic repulsion from the surfaces in closest proximity. At 25 nm separation (Figure 6b), the probe particle encounters a repulsive interaction (shown as emerging red contours) with the largest roughness peaks.

As the probe particle is brought to about 10 nm from the mean-plane of the surface (Figure 6c), the repulsive interactions intensify around the protrusions. There is also some physical overlap of the probe particle with the protrusions on the surface as indicated by the emergence of the underlying gray-scale map. Since the primary minimum immediately follows the repulsive energy barrier, there is an immediate transition from red to blue contours as a particle nears contact with the protrusions. Careful inspection of the figure reveals that the gray subdomains are immediately circumscribed by blue shaded contours, indicating that the interaction energy in the immediate periphery of these asperities is highly attractive, and hence, in these regions the particle center exists in the primary minimum of the DLVO energy profile.

Finally, as the probe is brought to 5 nm from the surface (Figure 6d), the entire mean-plane of the surface presents a fairly uniform repulsive energy barrier for the probe, interspersed with a few isolated regions containing the protruding hemispheres (peaks). During the entire vertical trajectory of the particle, the depressions on the rough surface do not appear to influence the overall interaction energy. Rather, it is the membrane surfaces in closest proximity to the probe particle that dominate manifestation of repulsive and attractive interactions as the particle approaches a rough surface. It will be shown that depressions (valleys) in the rougher surfaces play a marked role in colloid–membrane interactions.

Figure 7 depicts the corresponding interaction energy maps for a rough surface simulated on the basis of statistical parameters representing the NF70 membrane. The most prominent departure in Figure 7a–d from the plots of Figure 6 is the marked influence of the protruding asperities on the NF70 membrane even at a large separation distance of 50 nm (Figure 7a). The asperities of this membrane are comparable in dimensions to the probe particle, and hence, the particle “feels” the presence of these asperities at a much larger separation distance from the mean-plane. In contrast to Figure 6, the colloid probe encounters a considerably larger fraction of the

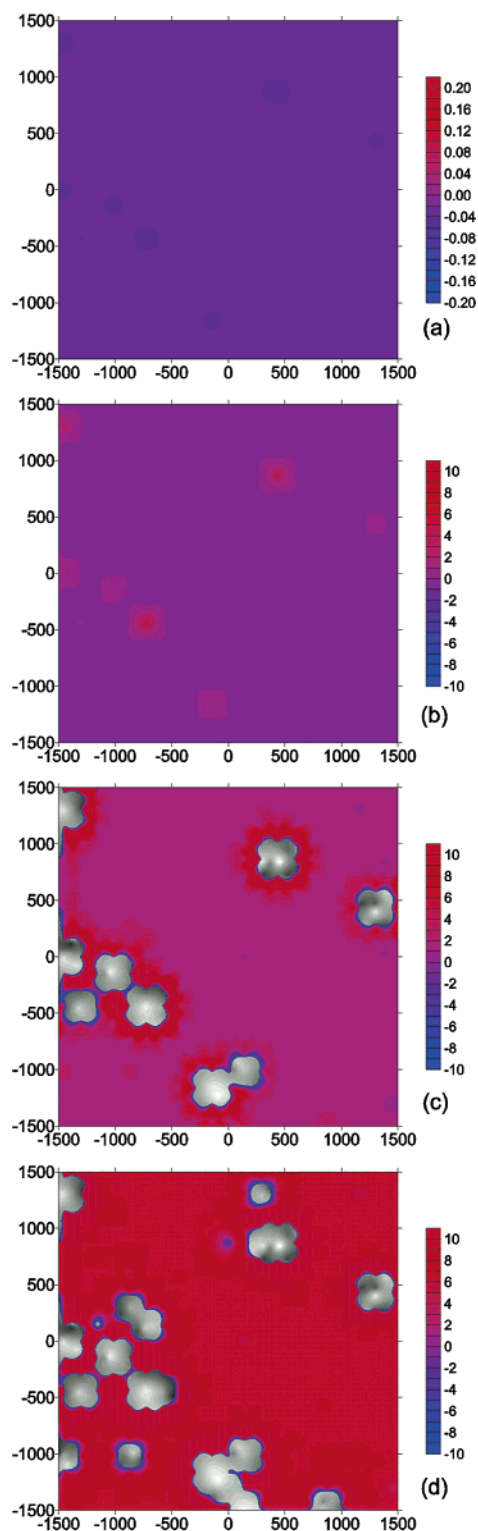


**Figure 6.** Interaction energy maps for a 50 nm (radius) particle approaching the simulated HL surface at separation distances of (a) 50, (b) 25, (c) 10, and (d) 5 nm. Solution chemistry and surface potentials were identical to those listed in Figure 5. The surface image has the same  $X$ - and  $Y$ -scales as Figure 4 yielding a  $9\ \mu\text{m}^2$  surface area. Blue color indicates negative (attractive) interaction energy, purple is neutral ( $0\ kT$ ), and red is positive (repulsive) interaction energy. The energy scale in (a) is reduced to reveal the magnitude of long-range attraction over most of the smooth surface. The interaction energy scales at the right of the other figures (b–d) are for the range of  $\pm 10\ kT$ . The gray-scale regions in (c) and (d) represent areas excluded from interaction energy calculation due to the presence of an interfering positive asperity that prevents the particle from occupying that  $x_c, y_c$  location.

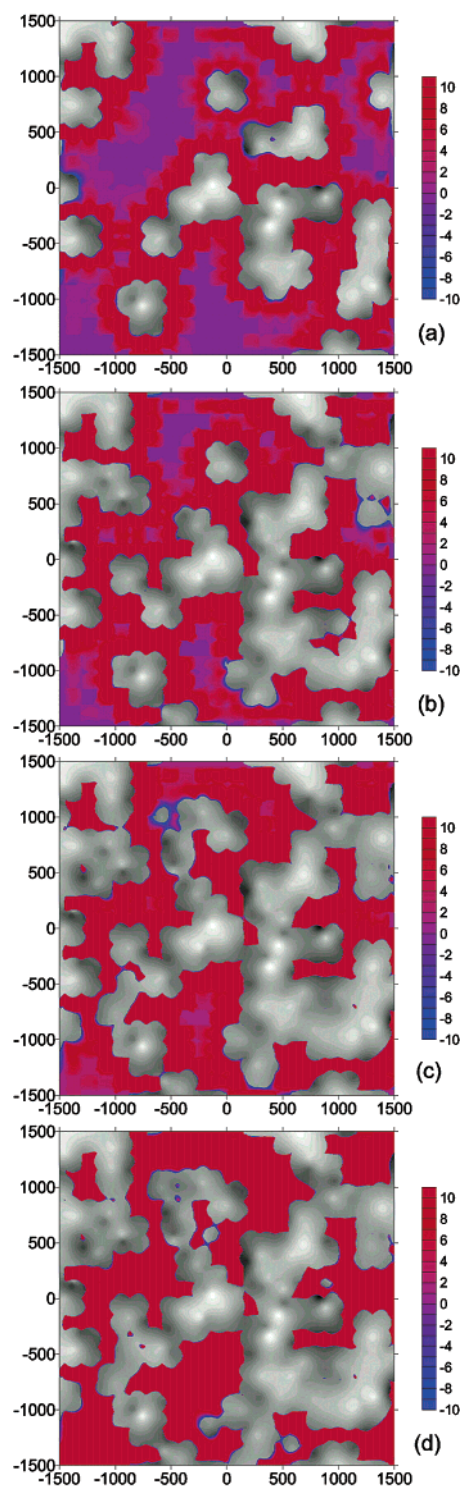


**Figure 7.** Interaction energy maps for a 50 nm (radius) particle approaching the simulated NF70 surface at separation distances of (a) 50, (b) 25, (c) 10, and (d) 5 nm. All simulation conditions were consistent with those in Figures 5 and 6.

surface that either is physically inaccessible or is repulsive even at large separations from the mean-plane.

The local interaction energy patterns in Figure 7 may suggest that a particle approaching a rough surface gets trapped in low-energy pockets (valleys) surrounded by domains of repulsive interaction (peaks). As the particle approaches closer to the surface, its lateral movement is restricted by the presence of the peaks, and eventually, the particle will deposit in a valley of the rough surface.



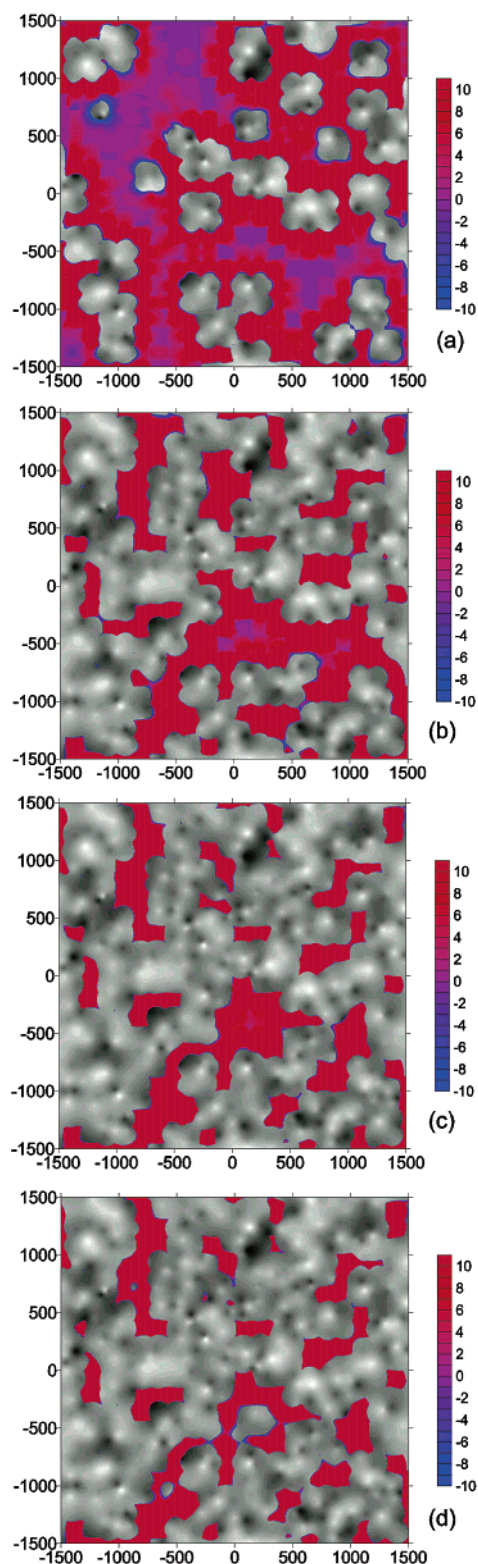


**Figure 8.** Interaction energy maps for a 50 nm (radius) particle approaching the simulated X20 surface at separation distances of (a) 50, (b) 25, (c) 10, and (d) 5 nm. All simulation conditions were consistent with those in Figures 5–7.

Furthermore, some particles may attach to the sidewalls of the asperities if they are forced to cross over the energy barrier and into the primary minimum due to physical interference of the neighboring asperities. This behavior is an outcome of the interplay between the DLVO and the physical (or steric) interactions that lead to complex particle deposition phenomena on rough membranes.

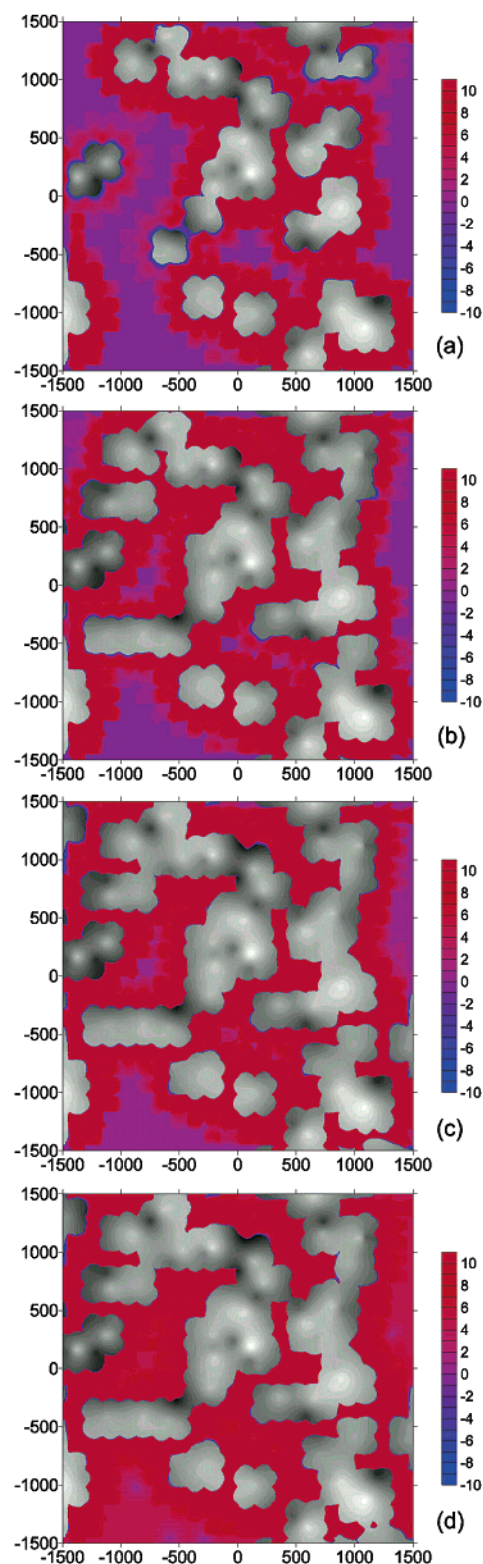


**Figure 9.** Interaction energy maps for a 50 nm (radius) particle approaching the simulated LFC1 surface at separation distances of (a) 50, (b) 25, (c) 10, and (d) 5 nm. All simulation conditions were consistent with those in Figures 5–8.

Figures 8 and 9 show the interaction energy maps for model surfaces emulating the X20 and LFC1 membranes, respectively. The general trends are similar to those observed in Figure 7 for a rough membrane. There are, however, subtle differences owing to the nature and distribution of the asperities between these cases. Notably, the X20 membrane (Figure 8) appears to be fairly inaccessible and uniformly repulsive as far away from



**Table 4. Measured and Simulated Membrane Statistical Roughness Parameters (Spheroids)**

| morphological parameter           | units           | HL               |                  | X20              |                  | NF70             |                  | LFC1             |                  |
|-----------------------------------|-----------------|------------------|------------------|------------------|------------------|------------------|------------------|------------------|------------------|
|                                   |                 | AFM <sup>a</sup> | SIM <sup>b</sup> | AFM <sup>a</sup> | SIM <sup>b</sup> | AFM <sup>a</sup> | SIM <sup>b</sup> | AFM <sup>a</sup> | SIM <sup>b</sup> |
| membrane area                     | $\mu\text{m}^2$ | 100              | 100              | 100              | 100              | 100              | 100              | 100              | 100              |
| number of asperities, $n$         | no.             | N/A <sup>c</sup> | 3084             | N/A <sup>c</sup> | 5680             | N/A <sup>c</sup> | 1899             | N/A <sup>c</sup> | 1107             |
| asperity shape factor, $\epsilon$ |                 | N/A <sup>d</sup> | 0.66             | N/A <sup>d</sup> | 0.68             | N/A <sup>d</sup> | 0.65             | N/A <sup>d</sup> | 0.65             |
| average roughness, $R_a$          | nm              | 10.1             | 10.2             | 33.4             | 33.4             | 43.3             | 44.4             | 52.0             | 54.4             |
| rms roughness, $R_q$              | nm              | 12.8             | 12.7             | 41.6             | 41.8             | 56.5             | 55.4             | 67.4             | 67.4             |
| maximum roughness, $R_m$          | nm              | 129              | 98               | 373              | 321              | 577              | 435              | 574              | 519              |
| peak count, PC                    |                 | 545              | 487              | 859              | 909              | 210              | 302              | 146              | 185              |
| surface area difference, SAD      | %               | 1.70             | 1.71             | 32.7             | 32.6             | 20.7             | 20.7             | 16.9             | 16.9             |

<sup>a</sup> Surface area scanned and analyzed by AFM. <sup>b</sup> Surface area reconstructed using hemispherical asperities. <sup>c</sup> The number of asperities in AFM surface scans was not available. <sup>d</sup> Not relevant for AFM surface roughness analysis.

the mean-plane as 25 nm. This is due to the narrow peak-to-peak separation distance for this membrane that physically bars the probe particle from sampling most of the membrane surface at separations of <25 nm. Finally, for the LFC1 membrane (Figure 9), we observe that the interaction energy is almost negligible at some regions of the surface even when the particle approaches close to the mean-plane (Figure 9c,d). This behavior can be attributed to the large peak-to-peak separation for this membrane that results from fewer, sparsely distributed large asperities, thus creating wide gaping valleys on the surface of LFC1.

The general trend observed from Figures 6–9 strongly indicates that a particle is both attracted and repelled more strongly by the protruding asperities on a rough membrane surface. However, as the particle approaches a rough surface, it may simply be funneled toward the valley regions of the surface. In the context of cross-flow membrane filtration, particles residing in the crevasses of rough membranes may be shielded from cross-flow shear by the large positive asperities, and thus initial particle deposition may be enhanced.

**4.3. Toward a More Accurate Representation of Membrane Surface Morphology.** It was noted in Table 2 that the simulated membrane surfaces based on hemispherical asperities provided statistical parameters that were somewhat lower than the AFM-based statistics for the real membrane surfaces. Furthermore, it might be an oversimplification to model a rough membrane on the basis of hemispherical asperities. In this context, we discuss a few possibilities for reconstructing a model rough surface that conforms more closely to the actual features and statistics of real rough surfaces. It should, however, be noted at the outset that the simplified calculations of the interaction energy will not be possible for the more general models of rough surfaces discussed subsequently. It is not primarily the computation of interaction energy that will be tedious for such models. Instead, it will be the detection and elimination of the projected surfaces of the membranes that physically interfere with the particle that will pose a constraint toward more accurate mapping of the interactions. For the case of hemispherical asperities, this particular task was simplified by the use of spherical symmetry.

A simple extension of the hemispherical asperity based model that could lead to better agreement with the experimental statistics would be to consider hemispherical asperities. A spheroid is the shape that results from rotating an ellipse about its major (oblate) or minor (prolate) axis. The shape factor or eccentricity of a spheroid ( $\epsilon$ ) is defined as

$$\epsilon = \sqrt{1 - \frac{b^2}{a^2}} \quad (8)$$

where  $b$  is the length of the minor axis and  $a$  is the length of the major axis of the ellipsoid. A sphere is the special case when  $a$  equals  $b$  ( $\epsilon = 0$ ).

The procedure of simulating a model rough surface with spheroidal asperities once again starts with the use of the AFM-measured  $R_a$  value as the average height of an asperity. The minor axis of the spheroid was determined by an initial guess for  $\epsilon$ . The surface area of the resulting hemispheroid determined the average asperity surface area. The AFM-measured SAD value was multiplied by the sample surface area ( $X \times Y$ ) and divided by the average asperity surface area to provide an initial guess for the number of asperities ( $n$ ). Following the case of hemispherical asperities, a random normal distribution of  $n$  values was generated with a mean equal to zero and unit standard deviation. Each value in the  $n$ -sized sample was multiplied by the AFM-measured  $R_q$  value. The surface area of each asperity of the distribution was calculated, and the sum was compared to the AFM-measured SAD values. The number of asperities was adjusted and the previous steps repeated, until the difference between simulated and measured (AFM) SAD values was minimized. The asperities were then randomly placed on the flat plate such that no asperity overlapped with another. The shape factors ( $\epsilon$ ) used as fitting parameters in the SIM membrane surfaces were 0.66, 0.65, 0.68, and 0.65 for HL, NF70, X20, and LFC1, respectively. These simulated surfaces were generated for the same projected surface area ( $100 \mu\text{m}^2$ ) as the AFM images of Figure 3.

Table 4 provides a glimpse of the improvement in the statistical parameters that can be attained by using spheroidal asperities. The roughness statistics calculated for the simulated membrane surface agree nearly perfectly with the AFM-derived roughness statistics for the real membranes. These results indicate that reconstruction of a rough surface can be performed quite accurately by increasing the number of adjustable parameters in the model. In case of hemispherical asperities, we had no freely adjustable parameters (only the asperity radius was varied employing a normal distribution), while in the model based on spheroidal asperities, the eccentricity was used as a second independently adjustable parameter.

The procedure of reconstructing a rough surface accurately can be refined further if the discrete topographic information from the AFM scans is directly fitted using bicubic splines or similar other piecewise functions. It is easily discernible that such reconstructions will lead to an almost exact match with the topography of the membrane surfaces. However, the added cost of computing the interaction of a single particle using such an approach might be quite prohibitive. In particular, one might be inclined to reconsider the usefulness of obtaining energy maps of such fine spatial resolution when considering the macroscopic behavior of a large membrane area. In particular, we should note that the calculation of the

interaction energy, as discussed here, is itself approximate. In this sense, it may not be prudent to obtain an exact geometric representation of the surface unless a more rigorous method of obtaining the electrostatic interactions is used in conjunction, for instance, via direct solution of the nonlinear Poisson–Boltzmann equation. The approach presented in this paper presents a significant advance toward a quantitative estimate of the extent to which surface roughness can affect colloid–membrane DLVO interactions. The simulation predictions provide a semi-quantitative understanding of the mechanism through which roughness influences colloid–surface DLVO interactions. Accounting for surface heterogeneities will no doubt lead to a more reasonable interpretation of the macroscopic deposition behavior of particles on rough surfaces, albeit in an average sense.

### 5. Concluding Remarks

The DLVO interaction energy between a spherical colloidal particle and a planar membrane surface is significantly altered by membrane surface morphology (roughness). The technique of employing statistical estimates of the surface topology based on atomic force microscopy in conjunction with surface element integration enables a detailed mapping of the interaction energy profiles of rough membrane surfaces for any particle size. Unlike the colloid-probe technique, this methodology allows consideration of very small particles, as well as

nanoscale roughness features on the membrane. The statistical nature of the analysis allows exploring the detailed relationship of the interaction energy profile to the surface topology and provides considerable insight into the role of such interactions on the macroscopic particle deposition behavior.

The primary influence of roughness is to reduce the repulsive energy barrier height, thus rendering rough surfaces more favorable for particle deposition. The complex, roughness-engendered interaction energy maps suggest that as particles approach closer to the membrane, they have a high probability of getting trapped in the valleys of the rough membrane. In addition, the presence of an attractive energy well (due to the van der Waals attraction) immediately surrounding each protruding asperity suggests that a more complex interplay between colloidal and physical (steric) interactions exists, which is absent on smooth surfaces. The results from this study, although semiquantitative, provide significant insight into how roughness influences the behavior of colloidal interactions between a particle and a surface at close proximity and how complex deposition behaviors can arise from such interactions.

**Acknowledgment.** The authors acknowledge the support of the National Science Foundation (Grant BES 0114527).

LA027083C